

Article

Insights into Interfacial Features of Metal/Eco-Composites Designed for Energy Storage

Raluca Marinica Albu , Andreea Irina Barzic , Mihai Asandulesa , Bogdan-George Rusu , Iuliana Stoica * 
and Ion Sava * 

“Petru Poni” Institute of Macromolecular Chemistry, 700487 Iasi, Romania; albu.raluca@icmpp.ro (R.M.A.); irina_cosutchi@yahoo.com (A.I.B.); asandulesa.mihai@icmpp.ro (M.A.); rusu.george@icmpp.ro (B.-G.R.)
* Correspondence: stoica_iuliana@icmpp.ro (I.S.); isava@icmpp.ro (I.S.)

Abstract: The development of innovative materials with improved properties is required for the field of energy storage. This article proves that it is possible to utilize bio-derived fillers to tune the performance of biodegradable polymers. For this scope, eco-composites were attained by loading several amounts of walnut leaf powder (WLP) in hydroxyethylcellulose (HEC). Basic testing was conducted to emphasize the sample’s suitability for the pursued application. The rheological behavior was altered with the addition of WLP at low shear rates, which became more pseudoplastic, resulting in composite films with higher thickness uniformity. Wettability characteristics were used to analyze the macro-level adhesion of the platinum-containing samples, and the results showed that the presence of WLP led to the augmentation of interfacial compatibilization of the composite with the metal layer. The electron microscopy and atomic force microscopy scans showed the proper distribution of the WLP in the matrix. Local adhesion data derived from DFL-height curves further showed that the inclusion of WLP improves the adhesion capabilities at the nanoscale. The dielectric spectroscopy tests proved that the used biofiller leads to an enhancement in the permittivity of the composite with respect to the neat HEC. By accounting for all results, the generated eco-composites are suggested as alternative dielectrics for usage in the energy storage domain.

Keywords: eco-composites; metallization; morphology; adhesion; dielectric behavior



Citation: Albu, R.M.; Barzic, A.I.; Asandulesa, M.; Rusu, B.-G.; Stoica, I.; Sava, I. Insights into Interfacial Features of Metal/Eco-Composites Designed for Energy Storage. *Coatings* **2023**, *13*, 1390. <https://doi.org/10.3390/coatings13081390>

Academic Editor: Xuanpeng Wang

Received: 30 June 2023

Revised: 28 July 2023

Accepted: 4 August 2023

Published: 8 August 2023



Copyright: © 2023 by the authors. Licensee MDPI, Basel, Switzerland. This article is an open access article distributed under the terms and conditions of the Creative Commons Attribution (CC BY) license (<https://creativecommons.org/licenses/by/4.0/>).

1. Introduction

Polymer-based coatings are widely studied owing to their advantageous flexibility, versatile shaping, and resistance to corrosion [1], which are explored in a multitude of applications. To render additional properties, the reformulation of coatings is needed, and this is performed with chemical modification [2] or the insertion of particular additives [3,4]. The conjunction of polymer performances with those of micro/nano-particles is widely investigated, especially for enhancement of the electrical [5] or thermal conduction [6] and also for improving the dielectric constant (ϵ) [7]. High-permittivity insulating materials are useful for manufacturing components for energy storage systems. The principal element of a capacitor is represented by the polymer dielectric medium. However, the majority of macromolecular compounds do not fulfill the requirement of $\epsilon > 3$, so they are doped with fillers that augment the molecular polarizability of the corresponding composite [8]. The most utilized fillers of polymer-based dielectrics for such purposes are ceramic [9], semiconducting oxides [10], metal [11], and carbon [12], which enhance the polarization behavior and hence the permittivity. To attain a more powerful polarization, the solution relies on larger interfacial domains, so nanofillers are preferred, but bulk dielectric properties are not the same at the nanoscale. A clear example is that of barium titanate, which is a ceramic having a permittivity in bulk of about 5000, and this value is reduced as the grain dimension is changed from microns to nanometers [13]. In addition to this, the inorganic particles lack biodegradability, and this affects the environment after the device’s lifetime

ends. Also, the insertion of nonmetal fillers into polymers limits the processability and mechanical performance of the composites, while metallic fillers have the drawback of augmenting the leakage current [8].

A less addressed topic is that of improving the dielectric characteristics of polymers by loading them with bio-based additives. Lee and Chang [14] studied the role of mica in enhancing the permittivity of polypropylene while diminishing the dielectric loss. A few reports deal with the role of bentonite on the dielectric behavior of modified poly(ϵ -caprolactone) [15] and polypyrrole [16], showing that this clay is suitable for rendering higher permittivity of the composites. Wood ash seems to be another important additive for producing polymer composites with increased permittivity [17]. Since the literature reports on this domain are not abundant, there are many opportunities to test other sorts of bio-originating materials for high- ϵ polymer composites. For instance, walnut is known to contain iodine, which is a highly polarizable molecule. When polymers are doped with iodine, the material's dielectric constant increases [18]. Iodine is abundantly found in nature walnut kernels, shells, and leaves. These biomaterials contain additional components that might be advantageous for increasing the polymer's permittivity, but this possibility has not been studied yet. The leaves of the European walnut are made of ellagitannins, phenolic acids, and flavonoids [19]. The incorporation of walnut leaf powder (WLP) into biodegradable polymers seems to be an intriguing pathway for designing green materials with tuned dielectric features for targeted applications.

To prepare high- ϵ dielectric composites that are not damaging to the environment, it is desirable to use polymers characterized by good biodegradability. Cellulose ethers, such as hydroxyethylcellulose (HEC), appear to be an optimal choice for this purpose since they are soluble in non-toxic solvents, display excellent film-forming capacity, and have huge mechanical flexibility. Due to its range of properties, HEC is broadly used in biomedicine, agriculture, cosmetics, membranes, food, and so on [20,21]. The involvement of this biodegradable polymer in energy storage uses is less examined in the literature. The few available studies suggest that the insertion of NH_4Br or NaPF_6 salt into HEC leads to electrode separators for batteries [22,23], while KCl-assisted compounding of HEC is adequate for adapting the electrochemical features of supercapacitors [24]. Other recent reports show that HEC is suitable for electrolytes formulations (derived using association with other polymers and fillers/salts/acids) in a gel state for capacitors or supercapacitors [25,26] and in a solid state for Zn batteries [27]. When fabricating capacitors, it is necessary to ensure uniformity in the dielectric layer thickness. To achieve this, the solution processing should be performed in precise conditions that are extracted from the rheological behavior [28–31]. There is a strong relationship between the material thickness and resulting morphology [32]. The latter affects the adhesion between the dielectric [33,34] and neighboring metallic layer from the capacitor structure. Their good compatibility is vital to ensure the desired device operability.

Given the illustrated context, this paper provides an original scientific method for making eco-compatible composites by exploring the possible advantages introduced with bio-originating compounds regarding the dielectric performance of biopolymers. Thus, this study attempts to tune the dielectric properties of HEC by adding increasing amounts of WLP and analyzing the eco-composite performance for energy storage uses. Novel insights are extrapolated from the correlation between the composite microstructure (tested using rheological and morphological techniques) and the polarization mechanisms (elucidated from broadband dielectric spectroscopy). Another aspect that is new in this work resides in the evaluation of the micro/nanoscale interfacial compatibility of the reinforced HEC films with a conductive metal layer, which is relevant for capacitor construction and viability.

2. Materials and Methods

The cellulose ether, namely, hydroxyethylcellulose (HEC) type NATROSOL 250, was obtained from Hercules.

Walnut leaf powder (WLP) was used as filler for composite manufacturing in this work. The leaves were collected from trees in the autumn season when they naturally dried. Subsequently, they were ground to attain the biofiller powder.

The samples were obtained mainly using a mixing approach. The HEC matrix was weighted (~0.208 g) and solved in 5 mL water. Variable amounts of WLP were incorporated into an HEC aqueous solution to acquire the following gravimetric ratios: 5, 10, and 20 wt%. Hence, the acronyms for the samples are HEC, WLP/HEC 5, WLP/HEC 10, and WLP/HEC 20. All systems were homogenized using mechanical stirring for 5 h and then deposited on glass supports using the tape casting technique, followed by drying at 60 °C for 48 h. At casting speeds of 8 mm/s, uniform films were obtained with a thickness of 45 µm for HEC and 47 µm for WLP/HEC 20, as indicated using digital micrometer measurements.

The electrode metal layer was deposited on the HEC-based samples using the sputtering method. Thus, a fine-grained, homogeneous, robust, and stable platinum coating with a thickness of 6.3 nm was placed on the samples using a Leica EM ACE200 sputter coater device (Leica Microsystems, Vienna, Austria). The sputter current was 30 mA, the sputter time was 45 s, and the sputter rate was 0.14 nm/s.

Rheometry analyses were performed on Bohlin CS50 equipment (Malvern Instruments, Malvern, UK).

The wettability of the films was assessed with contact angle experiments using glycerol (Gly) and formamide (F) liquid drops on the sample surface.

The morphology of the systems was acquired with a scanning electron microscope (SEM), Verios G4 UC Type (Thermo Scientific, Brno, Czech Republic), using a backscatter electron detector—ABS (angular backscattered detector)—at an accelerating voltage of 5/10 kV for better topographic contrast.

Atomic force microscopy (AFM) tests were conducted using an NTEGRA multifunctional Scanning Probe Microscope (NT-MDT Spectrum Instruments, Zelenograd, Moscow, Russia). The morphological aspects were evaluated in tapping mode, using an NSG10 cantilever, produced by NT-MDT Spectrum Instruments, Zelenograd, Moscow, Russia, having the following characteristics: tip curvature radius of 6 nm, resonant frequency of 243 kHz, and force constant of 6.2 N/m. The adhesion force between platinum and the surface of the samples was evaluated using the retract DFL–height curves (where DFL is the deflection of the cantilever), using force spectroscopy in contact mode. The cantilever used for this kind of measurement was NSG10/Pt, manufactured by TipsNano Co, Tallinn, Estonia. The specific features of this scanning probe were a tip curvature radius of 35 nm, tip side platinum coating layer of 20–30 nm, resonant frequency of 198 kHz, and force constant of 18 N/m. The type of the xy point set was a 5 × 5 grid. In this way, 25 force–distance curves were measured for the HEC and WLP20/HEC samples over a scanning area of 5 × 5 µm².

Dielectric analysis was conducted using a broadband dielectric spectrometer (Novo-control Technologies, Montabaur, Germany) functioning in connection with the Alpha-A analyzer.

Electrical breakdown experiments were performed using a lab-made device accounting for international standards (IEC 60243–1 (1998) and IEC 60243–2 (2001)). The sample thickness was determined using a high-precision digital micrometer. The samples were introduced between two spherical electrodes, and the breakdown was evaluated at the point of contact by setting a stepwise varying voltage (50–100 V/step).

3. Results and Discussion

The preparation of solid uniform coatings involves a deep examination of the shear response of the material in the fluid phase, as analyzed using rheology. The influence of the bio-derived filler on the polymer morphology is examined using microscopy techniques, emphasizing the homogeneity of the samples. For the implementation of the studied eco-composites in energy storage systems (i.e., capacitors), it is necessary to attain proper metal/dielectric adhesion and an enhanced dielectric constant. This balance of properties is detailed in the next sections of this paper.

3.1. The Influence of Shear Flow Behavior on Coating Uniformity

The coating ability of leveling is considerably affected by the rheological behavior of the samples. Viscosity tests were undertaken to observe the changes caused by the insertion of WLP into the HEC aqueous solutions. The recorded viscosity and shear stress dependencies on the imposed shear rate are illustrated in Figure 1a,b, respectively.

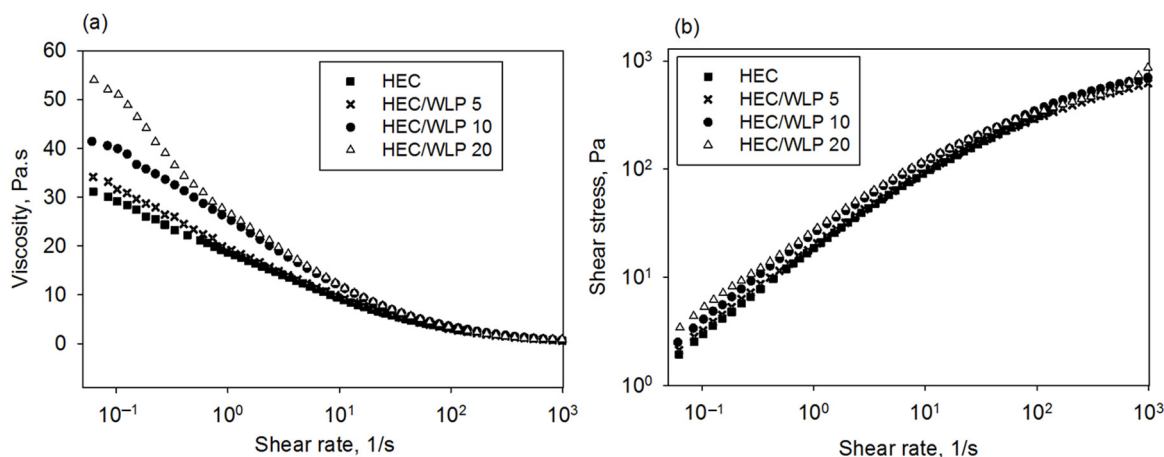


Figure 1. The viscosity (a) and shear stress (b) dependencies on the imposed shear rate for the HEC and WLP/HEC systems.

The investigated systems display no zero-shear viscosity plateau, regardless of the filler amount. When no shear is applied, the cellulosic chains are intertwined and entangled. Knowing that the entanglements oppose the flow, under approximately static conditions, the resistance to flow could be found at the highest level and, as a result, the zero-shear viscosity might be assessed at the smallest shear rate. Therefore, the differences in the viscosity curves upon the addition of WLP into HEC are particularly visible at shear rates below 10 s⁻¹. In this interval of shearing, the analyzed solutions present an increasing viscosity as the amount of the biofiller is increased in the matrix. The main components of the filler are biocompounds (e.g., ellagitannins, quercetin, kaempferol glycosides, and phenolic acids) containing oxygen-derived functionalities that are able to bind to hydroxyls from the HEC structure by hydrogen bonding, and hence, an increase the system's viscosity is noted. Across the entire shear rate interval of 0.06–1000 s⁻¹, one can notice a non-Newtonian behavior, meaning that the viscosity decreases upon higher shearing of the samples. The shear thinning behavior is characterized by two regions having distinct slopes. In the shearing domain of 0.06–10 s⁻¹, the viscosity ranges more suddenly since the macromolecules are aligning as a consequence of the imposed shear forces, and this diminishes the internal friction and hence the viscosity. In the range of 10–1000 s⁻¹, it seems that the slope of the viscosity curve is smaller, possibly because at this point, a smaller number of cellulosic chains remained that were still orientating during shear flow.

The shear stress curves are fitted using the power law proposed by Ostwald-Waele [35], as noted in Equation (1):

$$\sigma = C_i \dot{\gamma}^b \quad (1)$$

where σ —shear stress, C_i —consistency index, $\dot{\gamma}$ —shear rate, and b —the flow behavior index.

The linearization of Equation (1) is suitable for estimating the C_i and b parameters describing the shear flow of the samples. From the slope and intercept of the graphs displayed in Figure 1b, results for the shear flow and consistency indices were extracted and summarized in Table 1. It is widely recognized that a shear-thinning fluid has a flow index under unity, whereas a Newtonian liquid is characterized by $b = 1$, according to reports in the literature [28,36]. In this study, the results concerning the b parameter reveal that the flow index values decrease upon WLP introduction into HEC. This is probably due to the fact that the filler diminishes the interactions among the cellulosic chains and

favors their orientation during shear deformation. Moreover, the consistency in the system increases as the filler loading into HPC is enhanced.

Table 1. The attained results for the shear flow index (b) and consistency index corresponding to the HEC and WLP/HEC systems.

System	b	$C_i, \text{Pa}\cdot\text{s}^b$
HEC	0.77	17.87
WLP5/HEC	0.73	18.41
WLP10/HEC	0.72	23.23
WLP20/HEC	0.68	25.59

The oscillatory experiments provide data on the viscoelasticity of the samples. The shear moduli variations with frequency for all systems are depicted in Figure 2. All examined solutions present a transition from viscous to elastic flow. In the zone of small frequencies (up to 9 Hz), the viscous modulus is larger than the elastic modulus. Also, here, the shear moduli dependencies on the frequency are fitted using the power law, as shown in Equations (2) and (3):

$$G'' \sim f^1 \quad (2)$$

$$G' \sim f^2 \quad (3)$$

where G'' —viscous modulus, G' —elastic modulus, and f —shear frequency.

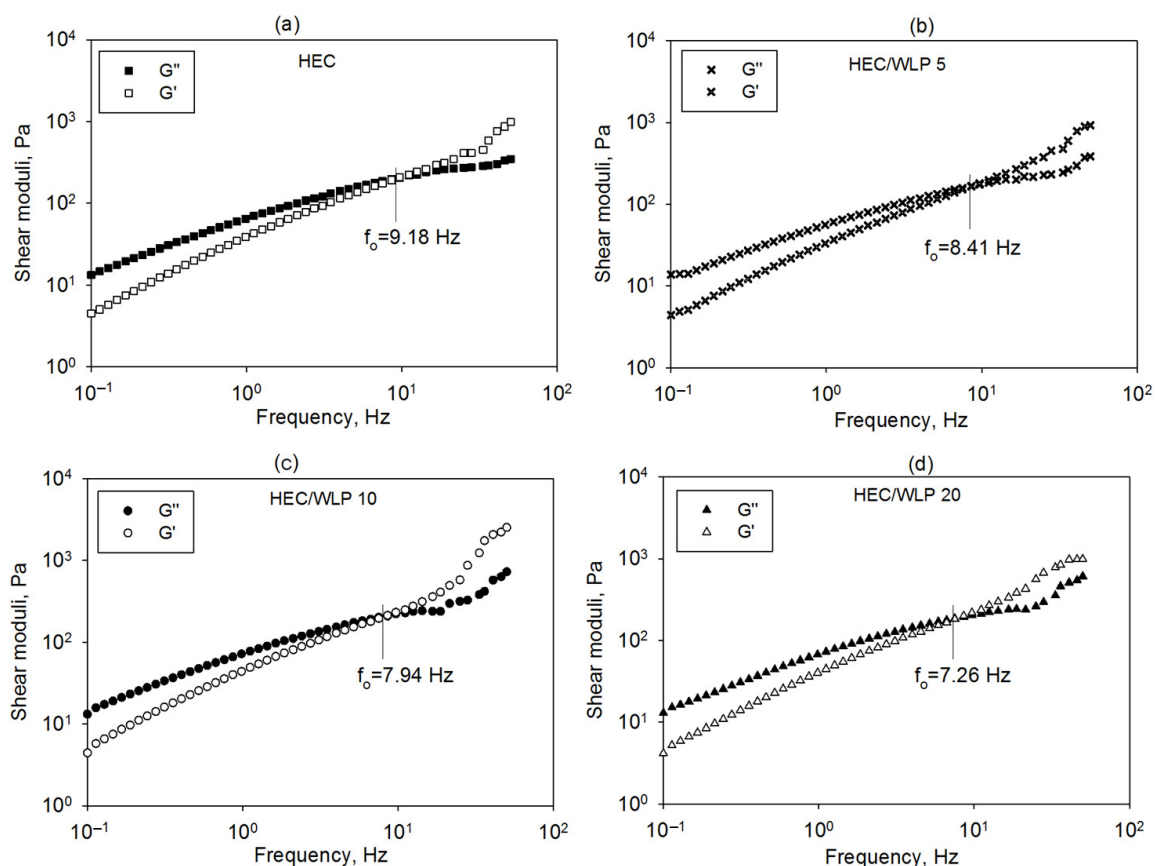


Figure 2. The shear moduli variation with frequency for the (a) HEC, (b) WLP5/HEC, (c) WLP10/HEC, and (d) WLP20/HEC systems.

These aspects are commonly encountered with viscoelastic fluids, as revealed by data in the literature [36]. For such fluids, there is a point where the elastic component gradually

increases and then exceeds the viscous component. The frequency denoting the equality between G'' and G' is known as the overlapping frequency (f_0). As observed in Figure 2, this parameter varies with the system composition.

In other words, the overlapping frequency is slightly diminished with the incorporation of the biofiller into the polymer, namely, 9.18 Hz for HEC, 8.41 Hz for WLP5/HEC, 7.94 Hz for WLP10/HEC, and 7.26 Hz for WLP20/HEC. The crossing point of the shear moduli from Figure 2 are important because they reveal the transition from viscous to elastic flow for the samples. The reverse of the crossing frequency is the relaxation time. The imposed deformation produces anisotropy, and the process to regain the initial state is based on the relaxation of the sample until the overall isotropic state is attained. Since f_0 decreases upon reinforcement, it appears that the relaxation time of the composite increases, and this is characteristic for solid-like behavior.

The flow curves are essential for predicting the quality of the coating leveling upon deposition with tape casting. Tape casting or the doctor blade method is a procedure for making polymer films by casting a solution layer on a support, and then the leveling of the solution is performed with a moving blade. Since the shape of the viscosity graph for the HEC solution does not differ much from those for the composites, only the processing conditions for the matrix and composite with 20 wt% filler are further analyzed. During the processing of polymer liquids with this method, the viscosity varies when coming out of the reservoir and when it is leveled with the blade. This is why the shear response of the samples influences the coating uniformity in terms of thickness. Comparing the data from Figures 1 and 2, it appears that a more pronounced shear thinning flow produces less variation in thickness using the blade casting processing, namely, for the HEC sample, the thickness variation is 0.32 μm , while for the WLP20/HEC sample, the thickness change is 0.21 μm . The analysis of the deposition must consider the forces involved in the processing stage, namely, the pressure-induced flow and drag-driven flow. Jabbari [37] constructed model to examine the implications of the effects arising from the shear rate and the pressure-related flow. It is paramount to account for the fact that the casting speed is strongly linked to the velocity profiles under the blade. This aspect is expressed in Equation (4):

$$v_x = v \frac{z}{h} + h^2 P \frac{z}{h} \cdot \left(1 - \frac{z}{h}\right) \quad (4)$$

where z —a coordinate of the Cartesian system along the fluid height, h —casting gap, v —draw velocity, and P —a parameter connected to the flow under pressure and certain geometrical features.

The rheological information registered for the samples was further linked to the velocity profiles during tape casting at variable casting speeds. The graphs illustrated in Figure 3a,b shows that when applying distinct draw velocities, the shape of the velocity curves below the casting blade is different. The shape of the obtained graphs is far from parabolic (typical for hydrostatic pressure effects). Thus, it can be noted that the linear aspect of the velocity profiles for the samples is linked to the dominant drag flow. It appears that the WLP reinforcement of HEC does not have much of an effect on the curves of velocity depicted in Figure 3.

The following step is focused on an evaluation of the interval of shear rates at which the samples are affected during blade casting. Such aspects are highly relevant because the modification of velocity is transferred into a scattering of the shear rate values. According to Figure 4a,b, the HEC and WLP/HEC systems present distinct local shear rates. For the HEC solution, it is found that as the casting speed increases, the local shear rate increases from 5.06 to 50.07 s^{-1} . A similar trend is observed for the WLP/HEC sample, but the shear rates acting under the blade are a bit smaller (5.03–50.04 s^{-1}). Selecting this shear interval from the rheological data, it is possible to understand the manner in which sample viscosity is modified during processing, meaning that the studied systems are shear thinning fluids in that range.

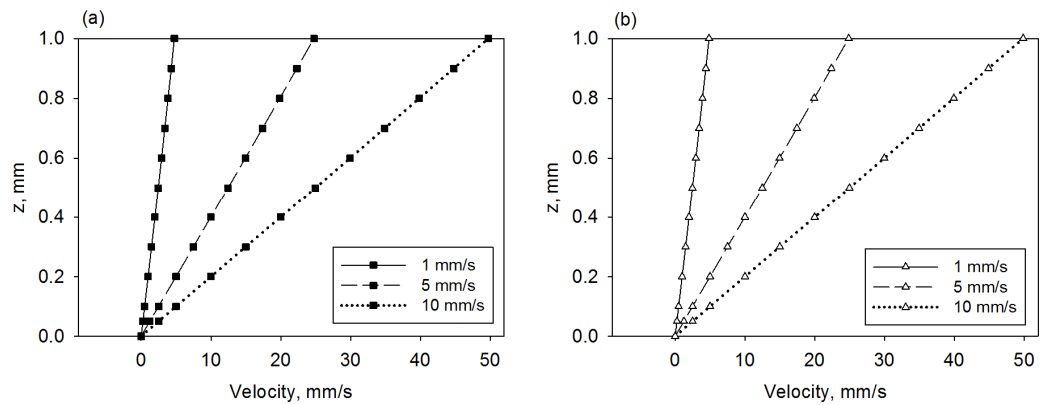


Figure 3. The velocity profiles below the casting blade for the (a) HEC and (b) WLP20/HEC systems.

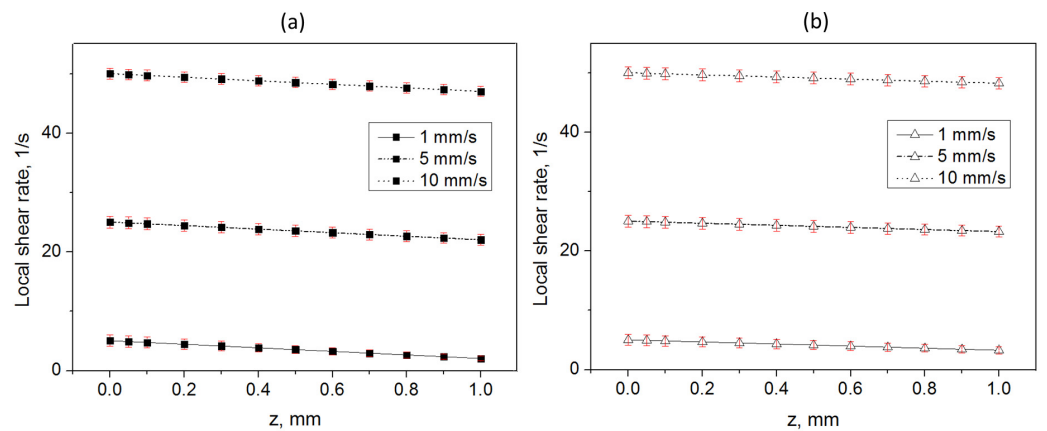


Figure 4. Local shear rate distributions below the blade for the (a) HEC and (b) WLP20/HEC systems.

To elucidate the relationship between the leveling of samples in the process of tape casting, the thickness variation was analyzed at several casting speeds. For this purpose, the model reported by Tok et al. [38] was used. This approach enables a connection between the coating thickness and rheological data expressing the shear thinning and fluid consistency, as shown in Equation (5):

$$t = \left[0.5 h + \frac{2(h/2)^{\frac{1}{2+b}} (\Delta P)^{\frac{1}{b}}}{LU(1/b + 2)C_1^{\frac{1}{b}}} \right] \frac{\alpha\beta\rho_s}{\rho_t} \tag{5}$$

where t —thickness, ΔP —pressure, U —blade speed, L —blade width, ρ_s —fluid density, ρ_t —tape density, α and β —correction factors [37].

During the casting stage, the solution is deformed as a consequence of the surface tension and thus, the viscosity is distinct at low and high coating speeds. Figure 5 shows how the thickness varies at several applied casting speeds for both studied systems. In the case of the HEC solution, the values of the t parameter decrease more abruptly between 1 and 5 mm/s in comparison with those attained for WLP20/HEC, which varies more significantly between 1 and 2 mm/s. The literature [37,38] supports the idea that the drag force is larger at increasing velocities, being an important effect with regard to the pressure force. As seen in Figure 5, for the HEC and WLP/HEC systems, it is remarked that at casting speeds beyond 2 mm/s and 5 mm/s, respectively, the impact of shear-driven flow on the coating thickness values is strong. The prepared WLP20/HEC eco-composite leads to a wider range of casting speeds where the coating thickness is uniform, as required for dielectrics used in energy storage.

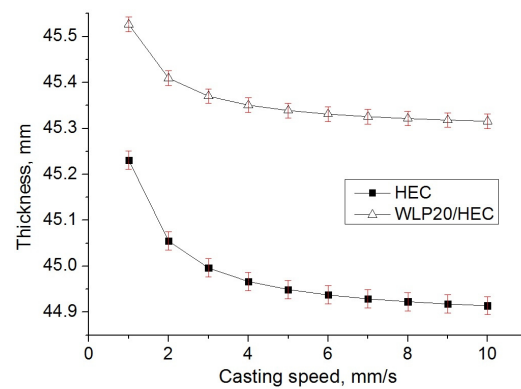


Figure 5. The thickness variation with casting speed for the HEC and WLP20/HEC systems.

3.2. Interfacial Adhesion with the Metal Layer

The interactions occurring at the interface of polymers and other contacting materials are dictated by the wettability characteristics. For the WLP/HEC composites, the polar and dispersive components of the surface tension are computed based on the contact angle (θ) measurements and Fowkes relation [39]:

$$1 + \cos \theta = \frac{2}{\gamma_l} \sqrt{\gamma_l^p \gamma_s^p} + \frac{2}{\gamma_l} \sqrt{\gamma_l^d \gamma_s^d} \quad (6)$$

where γ is the surface tension, the letters “p” and “d” symbolize the polar and dispersive components of the surface tension, and the indices “l” and “s” denote the liquid and solid phases, respectively.

In the above equation, the parameters corresponding to the measuring liquids are obtained from literature [40]. The contact angle and surface tension parameters values are illustrated in Table 2. The neat HPC film displays contact angle values around 60° , as reported in another study for another test liquid [41]. The insertion of WLP, which contains compounds rich in hydroxyl groups, leads to hydrogen bonding with the HEC matrix. This enhances the surface polar character, namely, larger γ_s^p values are attained upon progressive addition of the bio-derived filler. On the other hand, the dispersive contribution to the surface tension gradually decreases with the presence of WLP in HEC.

Table 2. The values of the contact angle, surface tension parameters (disperse and polar contributions), and work of adhesion with platinum for the WLP/HEC composites.

Sample Code	$\theta, ^\circ$		$\gamma_s^d, \text{dyn/cm}$	$\gamma_s^p, \text{dyn/cm}$	$W_a, \text{dyn/cm}$
	F	Gly			
HEC	60.0 ± 0.6	68.7 ± 0.6	29.2 ± 1.7	4.9 ± 0.9	73.2 ± 0.7
WLP5/HEC	62.7 ± 0.6	67.0 ± 0.0	18.6 ± 1.5	12.6 ± 1.1	76.2 ± 0.2
WLP10/HEC	65.7 ± 0.6	62.7 ± 0.6	5.7 ± 0.1	35.8 ± 0.2	82.7 ± 0.5
WLP20/HEC	70.0 ± 1.0	59.7 ± 0.6	0.2 ± 0.1	70.3 ± 2.8	88.0 ± 0.4

These data were further utilized to check how the composite would adhere to platinum, which is a common material used for the fabrication of electrodes. The work of adhesion (W_a) is a function of the surface tension parameters of the materials that come in contact, as expressed with the following equation:

$$W_a = 2 \cdot \left[\left(\gamma_s^d \cdot \gamma_m^d \right)^{0.5} + \left(\gamma_s^p \cdot \gamma_m^p \right)^{0.5} \right] \quad (7)$$

where the index m describes the metal phase.

The adhesion of the samples with platinum is quantified by W_a parameter, which is summarized in Table 2. It was found that the adhesion is intensified under loading HEC with increasing quantities of WLP. This might be attributed to the improvement in the polarity of the samples since the organic components from the WLP contain numerous hydroxyls. As supported by the literature describing the adhesion theory, the occurrence of functional groups, like hydroxyl and carboxyl, is beneficial for chemical bonding [42]. Thus, the supplementary -OH functionalities from the biofiller are favorable for enhancing the interfacial binding of the analyzed samples to the metallic phase.

3.3. Morphology and Local Adhesion Features

The surface morphology of the HEC matrix, WLP biofiller, and WLP20/HEC composite was first investigated using the SEM technique. According to the SEM micrographs presented in Figure 6, the surface of the HEC matrix is smooth and uniform and free of defects, observable both at a lower magnification of $150\times$ (Figure 6(a1)) and at a higher magnification of $1000\times$ (Figure 6(a2)). The general appearance of the WLP biofiller at the micrometric scale is presented in Figure 6b. To investigate the influence of the inclusion of bio-derived filler in the polymer matrix on the morphology, the WLP20/HEC composite sample was analyzed both on the surface (Figure 6(c1,c2)), as well as in the bulk, by examining the cross-section of the film (Figure 6d). These images emphasized the optimal and efficient embedding of the biofiller into the HEC matrix, leading to homogeneity in the composite by creating physical links between the two components. As a result, a certain structural organization can take place, and circular formations can be observed at the surface of the composite at a magnification of $1000\times$ (Figure 6(c2))

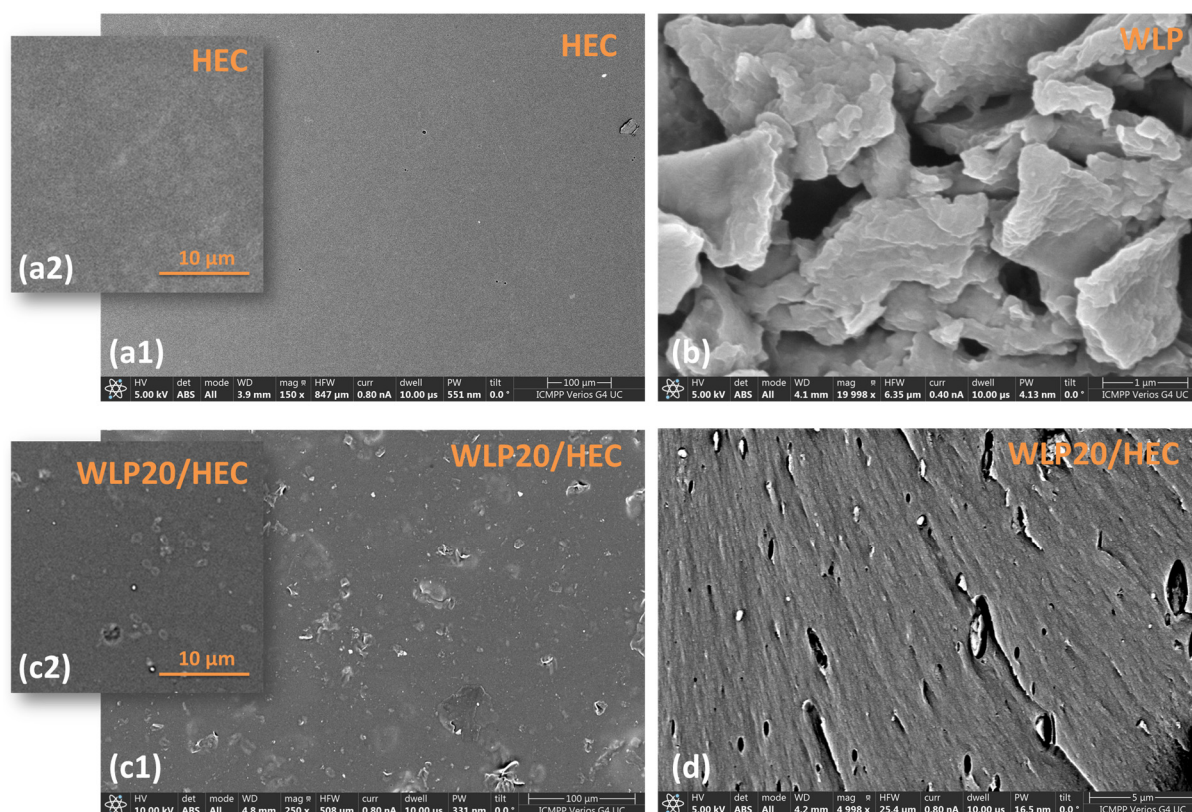


Figure 6. SEM images recorded for the HEC, WLP, and WLP20/HEC systems.

To analyze more deeply the morphology of the investigated systems, atomic force microscopy was used. The AFM (height and phase) images obtained with nanometric resolution are presented in Figure 7(a1–a3) for the HEC matrix sample and in Figure 7(b1–b3) for the WLP20/HEC composite. The AFM height images show that the surface of the

HEC matrix is very smooth; the maximum scanning points being at a height of not even 10 nm. It presents discrete pores with a diameter varying between 100 and 150 nm, which are uniformly distributed over the entire investigated surface. The average roughness calculated on the surface of $5 \times 5 \mu\text{m}^2$ does not exceed the value of 0.5 nm. The image with phase contrast (Figure 7(a3)) shows an extremely small phase shift between the furthestmost points, which indicate that the HEC matrix is uniform and consists of a single phase.

With the insertion of the WLP biofiller into the HEC matrix and the formation of the WLP20/HEC composite, the surface morphology at the nanometric scale changes considerably (Figure 7(b1,b2)). Thus, the appearance of large formations, even of 500 nm, of different sizes and shapes (globular or ellipsoidal), although not very well defined, can be observed. These cause the average roughness to increase considerably from 0.5 nm to 8.3 nm due to the increase in maximum heights up to 124 nm.

Due to the fact that in the phase contrast image (Figure 7(b3)), the formations appear with a considerable phase shift of over 50 degrees, it can be clearly concluded that these formations are represented by the WLP biofiller, and the background part can be attributed to the HEC matrix.

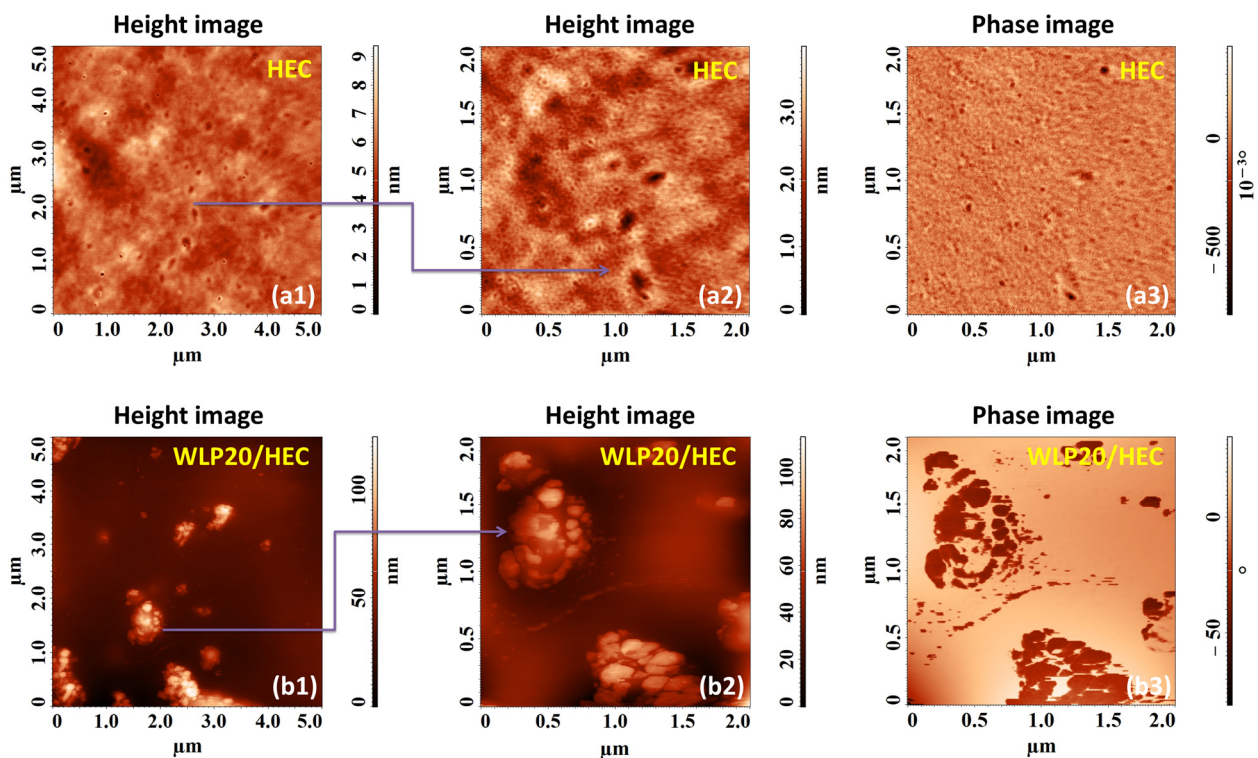


Figure 7. Height and phase AFM images recorded for the HEC and WLP20/HEC systems.

The average local nanoscale adhesion force between the covered NSG10 cantilever's tip with a platinum layer at a thickness of 20–30 nm and the HEC matrix and WLP20/HEC system was calculated using the blue retract DFL-height curves (presented in Figure 8a,b). This adhesion force computed using Hooke's law proved to be higher (even almost double) in the case of the WLP20/HEC composite due to the fact that the biofiller creates hydrogen bonds with the polymer matrix, thus increasing both the surface polarity and the polarizability in volume.

To test the efficiency of the deposition of the metallic phase both on the surface of the HEC matrix surface and on the WLP20/HEC composite, the sputtering method was used. The AFM analysis of the surfaces at the nano-scale performed after the deposition of the platinum layer is presented in Figure 9(a1–a3) for the HEC/Pt sample and in Figure 9(b1–b3) for the WLP20/HEC/Pt system. On the surface of the HEC matrix, the platinum particles, with an average diameter between 30 and 40 nm, were evenly distributed over the entire

area (Figure 9(a2)), covering the surface very efficiently. This was tested using the image obtained in phase contrast (Figure 9(b3)), which, due to the phase shift of several degrees, does not show the existence of two distinct phases on the surface but only one (the metallic one). This phase shift of a few degrees was recorded because of the height differences in the formations that make up the nanorelief. Due to the deposited metal layer, the maximum height increases to almost 40 nm, determining the augmentation of the average roughness to 1 nm.

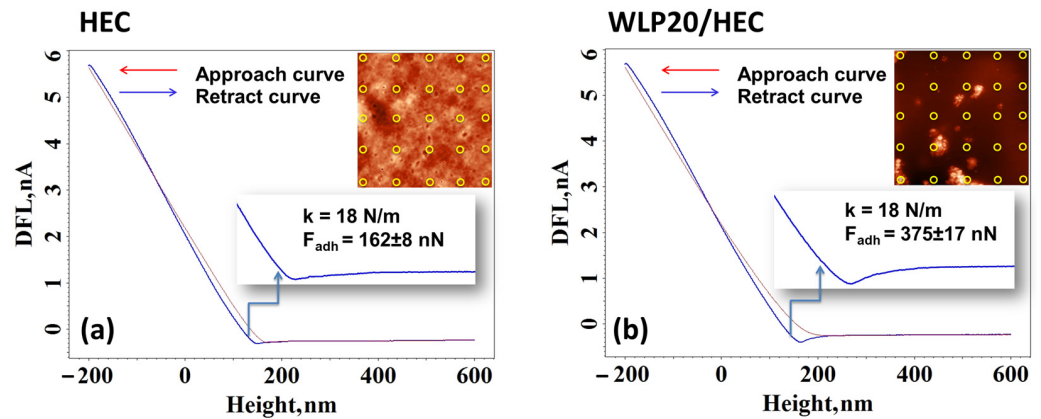


Figure 8. Typical DFL-height curves (red, approach curve; blue retract, curve) registered for the HEC matrix (a) and WLP20/HEC system (b). The place where each curve was collected is indicated on the AFM images inserted in the upper right corner.

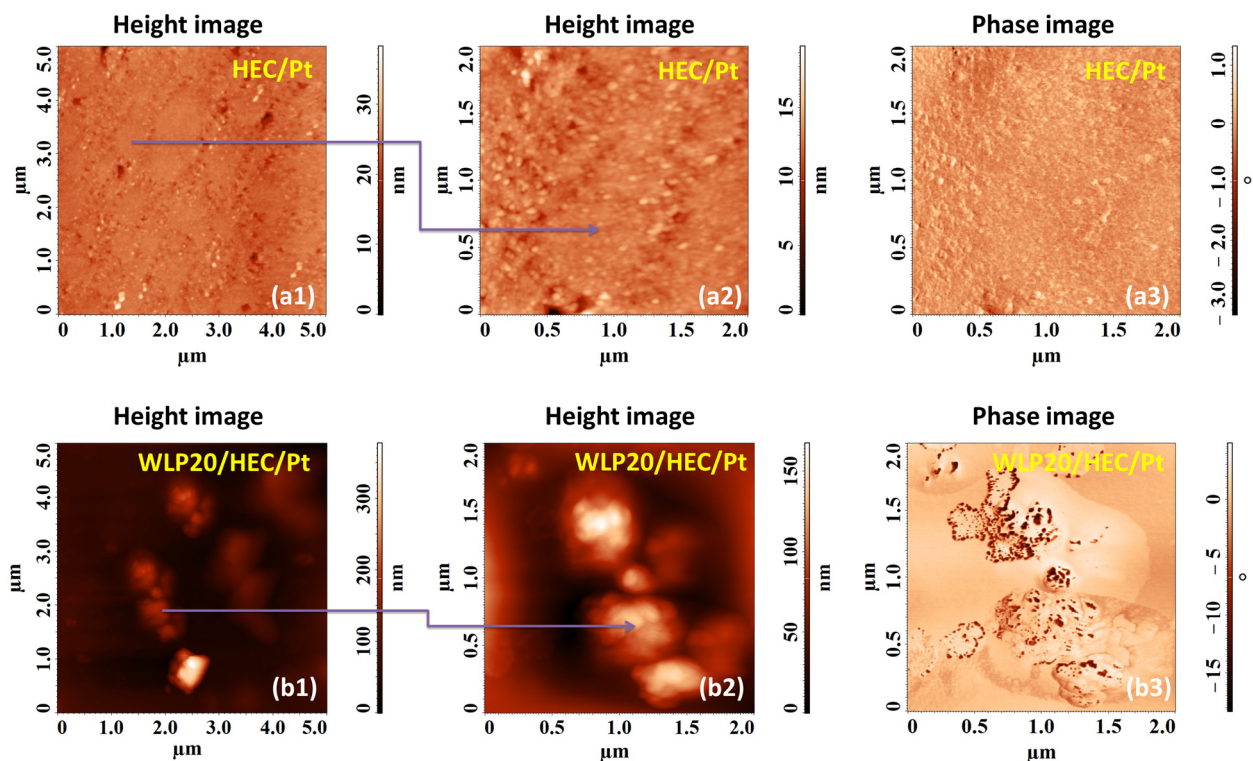


Figure 9. Height and phase AFM images recorded for the HEC/Pt and WLP20/HEC/Pt systems.

The platinum coating is also very good in the case of the WLP20/HEC/Pt system. The morphological aspect of the AFM images (Figure 9(b1,b2)) confirms a greater adhesion of the platinum than in the previous case. The deposited metallic layer, although it follows a rather complex morphology, can still be perceived as a unit since the individual platinum particles are not so visible. Regarding the image in Figure 9(b3), the phase contrast is

influenced by a rather low phase shift, of about 10–15 degrees, which indicates that the platinum layer should be thicker in this case, so the deposition time should be extended. The thickness of the metal deposition should be greater than 6.3 nm to better cover the formations of the surface relief, which are larger in the case of the WLP20/HEC system compared with HEC, where the roughness is very small and the morphology is uniform and homogeneous.

Regarding the texture amplitude parameters, they increase after the deposition of the metal layer. However, a comparison with the starting sample is not auspicious since the same types of formations are not captured on the images.

3.4. Dielectric Behavior

The dielectric behavior of most polymers can be tailored with the incorporation of certain additives. Using dielectric spectroscopic data collected at room temperature, it was possible to clarify the impact of the bio-originating filler on the development of the HEC-based composite permittivity. According to Figure 10, it is noticed that the presence of WLP causes an increase in the dielectric constant. Within the studied frequency interval, it is generally known that the occurring polarization mechanisms are dipolar and atomic, which overlap with electronic polarization. The enhancement in the permittivity is generated by the presence of the WLP components, which contain many hydroxyls, and render supplementary dipoles that contribute to the permittivity magnitude enhancement.

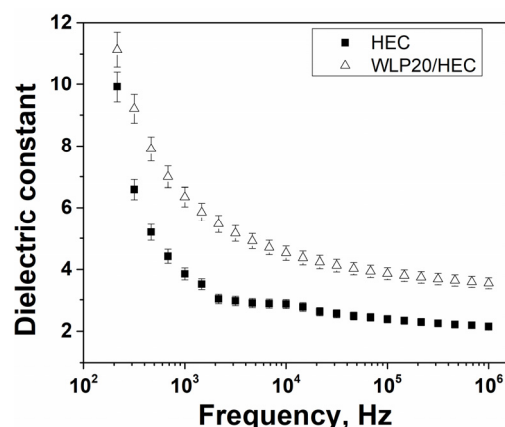


Figure 10. The dielectric spectra of HEC and WLP20/HEC samples at ambient temperature.

The breakdown characteristics of the samples were also measured. It can be observed in Table 3 that the breakdown voltage is influenced by the material composition. Accounting for the thickness of each studied film, it was possible to determine the breakdown strength (Eb). The results reveal that the incorporation of a higher quantity of WLP into HEC produces a slight reduction in the Eb parameter.

Table 3. The values of breakdown voltage (Vb), sample thickness, and breakdown strength (Eb).

Sample	Vb, V	Thickness, μm	Eb, V/ μm
HEC	2860	33	86.7
WLP5/HEC	2673	47	56.9
WLP10/HEC	2571	55	46.7
WLP20/HEC	2402	59	40.7

4. Conclusions

This work aimed to reveal the importance of bio-derived fillers in tailoring the morphological, adhesion, and dielectric performance of biodegradable polymers. In order to do

this, WLP was added to a cellulose derivative called HEC, and a basic characterization was carried out to determine the material's potential for energy storage. The shear flow characteristics became more pseudoplastic after inserting the WLP filler. This was transferred as less variation in the thickness profile of the composite films attained with the doctor blade procedure. The wettability measurements allowed for an evaluation of the adhesion work of the WLP/HEC samples with platinum electrodes, which indicated that interfacial compatibility is ensured with the addition of WLP. The homogeneity in the multicomponent material was checked using SEM scans, which proved a good distribution of the biofiller in the HEC medium. A platinum layer was deposited on the prepared composite, and the local adhesion was tested with AFM. The acquired information demonstrated that the addition of WLP resulted in improved adherence of the composite to the metal phase. Dielectric spectra showed that doping HEC with a filler rich in hydroxyls led to an increase in the dipolar polarization mechanisms and, implicitly, to a higher dielectric constant. It was concluded that these environmentally friendly composites can be suggested for energy storage applications due to the enhancement in composite–metal adhesion and dielectric performance.

Author Contributions: Conceptualization, R.M.A. and A.I.B.; methodology, R.M.A., A.I.B., M.A., B.-G.R. and I.S. (Iuliana Stoica); software, M.A. and I.S. (Iuliana Stoica); validation, R.M.A., I.S. (Iuliana Stoica), and I.S. (Ion Sava); formal analysis, R.M.A.; investigation, R.M.A., A.I.B., M.A., B.-G.R. and I.S. (Iuliana Stoica); resources, R.M.A., A.I.B., M.A., B.-G.R. and I.S. (Iuliana Stoica); data curation, R.M.A., I.S. (Iuliana Stoica) and I.S. (Ion Sava); writing—original draft preparation, R.M.A., A.I.B., M.A. and I.S. (Iuliana Stoica); writing—review and editing, R.M.A., A.I.B., M.A., I.S. (Iuliana Stoica) and I.S. (Ion Sava); visualization, R.M.A., I.S. (Iuliana Stoica) and I.S. (Ion Sava); supervision, R.M.A., I.S. (Iuliana Stoica) and I.S. (Ion Sava); project administration, R.M.A.; funding acquisition, R.M.A. All authors have read and agreed to the published version of the manuscript.

Funding: This research was funded by a grant from the Ministry of Research, Innovation and Digitization, CNCS—UEFISCDI, project number PN-III-P1-1.1-TE-2021-0762, within PNCDI III.

Institutional Review Board Statement: Not applicable.

Informed Consent Statement: Not applicable.

Data Availability Statement: All data that support the findings of this study are incorporated in the main manuscript. No additional data are available for sharing.

Conflicts of Interest: The authors declare no conflict of interest.

References

1. Smith, J.R.; Lamprou, D.A. Polymer coatings for biomedical applications: A review. *Trans. IMF* **2014**, *92*, 9–19. [[CrossRef](#)]
2. Sun, W.; Liu, W.; Wu, Z.; Chen, H. Chemical Surface Modification of Polymeric Biomaterials for Biomedical Applications. *Macromol. Rapid Commun.* **2020**, *41*, 1900430. [[CrossRef](#)] [[PubMed](#)]
3. Barzic, A.I.; Albu, R.M.; Stoica, I.; Hulubei, C. New shielding covers based on transparent polyimide/ferrous sulfide composites that reduce optical losses in solar cells. *Compos. Sci. Technol.* **2022**, *218*, 109140. [[CrossRef](#)]
4. Albu, R.M.; Avram, E.; Stoica, I.; Ioanid, E.G.; Ioan, S. Miscibility and morphological properties of quaternized polysulfone blends with polystyrene and poly(4-vinylpyridine). *Polym. Compos.* **2011**, *32*, 1661–1670. [[CrossRef](#)]
5. Fang, Q.; Lafdi, K. Effect of nanofiller morphology on the electrical conductivity of polymer nanocomposites. *Nano Express* **2021**, *2*, 010019. [[CrossRef](#)]
6. Barzic, R.F.; Barzic, A.I.; Dumitrascu, G. Percolation network formation in poly(4-vinylpyridine)/aluminum nitride nanocomposites: Rheological, dielectric, and thermal investigations. *Polym. Compos.* **2014**, *35*, 1543–1552. [[CrossRef](#)]
7. Zhou, T.; Zha, J.-W.; Cui, R.-Y.; Fan, B.-H.; Yuan, J.-K.; Dang, Z.-M. Improving Dielectric Properties of BaTiO₃/Ferroelectric Polymer Composites by Employing Surface Hydroxylated BaTiO₃ Nanoparticles. *ACS Appl. Mater. Interfaces* **2011**, *3*, 2184–2188. [[CrossRef](#)]
8. Zha, J.-W.; Zheng, M.-S.; Fan, B.-H.; Dang, Z.-M. Polymer-based dielectrics with high permittivity for electric energy storage: A review. *Nano Energy* **2021**, *89*, 106438. [[CrossRef](#)]
9. Barzic, A.I.; Soroceanu, M.; Rotaru, R.; Doroftei, F.; Asandulesa, M.; Tugui, C.; Dascalu, I.A.; Harabagiu, V. Cellulose derivative/barium titanate composites with high refractive index, conductivity and energy density. *Cellulose* **2022**, *29*, 863–878. [[CrossRef](#)]

10. Wen, F.; Zhu, C.; Li, L.; Zhou, B.; Zhang, L.; Han, C.; Li, W.; Yue, Z.; Wu, W.; Wang, G.; et al. Enhanced energy storage performance of polymer nanocomposites using hybrid 2D ZnO@MoS₂ semiconductive nano-fillers. *Chem. Eng. J.* **2022**, *430*, 132676. [[CrossRef](#)]
11. Li, S.; Dong, J.; Niu, Y.; Li, L.; Wang, F.; Hu, R.; Cheng, J.; Sun, L.; Pan, Z.; Xu, X.; et al. Enhanced high-temperature energy storage properties of polymer composites by interlayered metal nanodots. *J. Mater. Chem. A* **2022**, *10*, 18773–18781. [[CrossRef](#)]
12. Han, Q.; Sheng, Y.; Liu, X.; Zhang, X.; Chen, X.; Li, B.; Han, Z. Carbon fiber reinforced epoxy composite combining superior electrochemical energy storage and mechanical performance. *Chem. Eng. J.* **2022**, *437*, 135228. [[CrossRef](#)]
13. Almeida, G.N.; de Souza, R.N.; Lima, L.F.S.; Mohallem, N.D.S.; da Silva, E.P.; Silva, A.M.A. The Influence of the Synthesis Method on the Characteristics of BaTiO₃. *Materials* **2023**, *16*, 3031. [[CrossRef](#)] [[PubMed](#)]
14. Lee, C.-Y.; Chang, C.-W. Dielectric Constant Enhancement with Low Dielectric Loss Growth in Graphene Oxide/Mica/Polypropylene Composites. *J. Compos. Sci.* **2021**, *5*, 52. [[CrossRef](#)]
15. Pihtili, G.; Torğut, G.; Biryant, F. Electrical properties of two-armed poly(ϵ -CL-co-BMA) composites filled with bentonite. *J. Polym. Res.* **2020**, *27*, 156. [[CrossRef](#)]
16. Maw, A.M.; Theingi, M.; Yee, K.T. A Study on the Dielectric Properties of Polypyrrole-Bentonite Composites. *J. Myanmar Acad. Arts Sci.* **2019**, *XVII*, 581–598.
17. Elloumi, I.; Koubaa, A.; Kharrat, W.; Bradai, C.; Elloumi, A. Dielectric Properties of Wood-Polymer Composites: Effects of Frequency, Fiber Nature, Proportion, and Chemical Composition. *J. Compos. Sci.* **2021**, *5*, 141. [[CrossRef](#)]
18. Tiwari, M. Dielectric Investigations in Iodine Doped Polystyrene Thin Films. *Int. J. Adv. Res. Sci. Commun. Technol.* **2020**, *11*, 179–183. [[CrossRef](#)]
19. Matławska, I.; Bylka, W.; Widy-Tyszkiewicz, E.; Stanisław, B. Determination of the Juglone Content of Juglans regia Leaves by GC/MS. *Nat. Prod. Commun.* **2015**, *10*, 1239–1242. [[CrossRef](#)]
20. Noreen, A.; Zia, K.M.; Tabasum, S.; Khalid, S.; Shareef, R. A review on grafting of hydroxyethylcellulose for versatile applications. *Int. J. Biol. Macromol.* **2020**, *150*, 289–303. [[CrossRef](#)]
21. Huang, J.; Hua, L.; Song, L.; Li, J.; E., S.; Lu, Z. Hydroxyethyl cellulose/boron nitride nanosheet films coated with silver nanowires for electronic packaging applications. *Mater. Today Sustain.* **2023**, *21*, 100307. [[CrossRef](#)]
22. Azha, M.A.S.; Dannoun, E.M.A.; Aziz, S.B.; Kadir, M.F.Z.; Zaki, Z.I.; El-Bahy, Z.M.; Sulaiman, M.; Nofal, M.M. High Cyclability Energy Storage Device with Optimized Hydroxyethyl Cellulose-Dextran-Based Polymer Electrolytes: Structural, Electrical and Electrochemical Investigations. *Polymers* **2021**, *13*, 3602. [[CrossRef](#)] [[PubMed](#)]
23. Chavan, C.; Bhajantri, R.F.; Cyriac, V.; Ismayil; Bulla, S.S.; Sakthipandi, K. Investigations on anomalous behavior of ionic conductivity in NaPF₆ salt loaded hydroxyethyl cellulose biodegradable polymer electrolyte for energy storage applications. *Polym. Adv. Technol.* **2023**, *34*, 1698–1715. [[CrossRef](#)]
24. Kim, E.-K.; Chang, H.S.; Lee, B.-M.; Park, J.-J.; Yun, J.-M.; Choi, J.-H. KCl-assisted synthesis of hierarchically porous carbon materials from water-soluble 2-hydroxyethyl cellulose for high-performance green supercapacitors. *Sustain. Mater. Technol.* **2022**, *34*, e00520. [[CrossRef](#)]
25. Rosi, M.; Iskandar, F.; Abdullah, M. Khairurrijal Hydrogel-polymer electrolytes based on polyvinyl alcohol and hydroxyethylcellulose for supercapacitor applications. *Int. J. Electrochem. Sci.* **2014**, *9*, 4251–4256. [[CrossRef](#)]
26. Youssef, A.M.; Hasanin, M.S.; El-Aziz, M.E.A.; Turkey, G.M. Conducting chitosan/hydroxyethyl cellulose/polyaniline bio-nanocomposites hydrogel based on graphene oxide doped with Ag-NPs. *Int. J. Biol. Macromol.* **2021**, *167*, 1435–1444. [[CrossRef](#)] [[PubMed](#)]
27. Brige, A.; Olsson, M.; Xiong, S.; Matic, A. A comparative study of hydroxyethylcellulose-based solid polymer electrolytes for solid state Zn batteries. *Nano Sel.* **2023**, *4*, 102–111. [[CrossRef](#)]
28. Stoica, I.; Buruiana, L.L.; Albu, R.M.; Soroceanu, M.; Barzic, A.I. Rheological and optical response of hydroxypropyl methylcellulose under variable temperatures for optical switching based on thermo-optical effect. *Polym. Adv. Technol.* **2023**, *34*, 1245–1252. [[CrossRef](#)]
29. Albu, R.M.; Hulubei, C.; Stoica, I.; Barzic, A.I. Semi-alicyclic polyimides as potential membrane oxygenators: Rheological implications on film processing, morphology and blood compatibility. *Express Polym. Lett.* **2019**, *13*, 349–364. [[CrossRef](#)]
30. Barzic, A.I.; Soroceanu, M.; Albu, R.M.; Ioanid, E.G.; Sacarescu, L.; Harabagiu, V. Correlation Between Shear-Flow Rheology and Solution Spreading During Spin Coating of Polysilane Solutions. *Macromol. Res.* **2019**, *27*, 1210–1220. [[CrossRef](#)]
31. Barzic, A.I.; Albu, R.M.; Stoica, I.; Varganici, C.D.; Hulubei, C. Polyimides containing cycloaliphatic units and chalcogen atoms as alternative shielding coatings for solar cells. *Polym. Bull.* **2023**, *80*, 4503–4522. [[CrossRef](#)]
32. Kahouli, A. Effect of film thickness on structural, morphology, dielectric and electrical properties of parylene C films. *J. Appl. Phys.* **2012**, *112*, 064103. [[CrossRef](#)]
33. Iqbal, H.M.S.; Bhowmik, S.; Benedictus, R. Study on the effect of surface morphology on adhesion properties of polybenzimidazole adhesive bonded composite joints. *Int. J. Adhes. Adhes.* **2017**, *72*, 43–50. [[CrossRef](#)]
34. Soroceanu, M.; Barzic, A.I.; Stoica, I.; Sacarescu, L.; Ioanid, E.G.; Harabagiu, V. Plasma effect on polyhydrosilane/metal interfacial adhesion/cohesion interactions. *Int. J. Adhes. Adhes.* **2017**, *74*, 131–136. [[CrossRef](#)]
35. Siddiqui, A.A. On transient-flows of the Ostwald-de Waele fluids-transport in the Darcy-Brinkman porous medium. *AIP Adv.* **2017**, *7*, 075316. [[CrossRef](#)]
36. De Gennes, P.G. *Scaling Concepts in Polymer Physics*; Cornell University Press: Ithaca, NY, USA, 1979; ISBN 080141203X.

37. Jabbari, M.; Bulatova, R.; Hattel, J.H.; Bahl, C.R.H. Quasi-steady state power law model for flow of $(\text{La}_{0.85}\text{Sr}_{0.15})_{0.9}\text{MnO}_3$ ceramic slurry in tape casting. *Mater. Sci. Technol.* **2013**, *29*, 1080–1087. [[CrossRef](#)]
38. Tok, A.I.Y.; Boey, F.Y.C.; Lam, Y.C. Non-Newtonian fluid flow model for ceramic tape casting. *Mater. Sci. Eng. A* **2000**, *280*, 282–288. [[CrossRef](#)]
39. Fowkes, F.M. Attractive forces at interfaces. *Ind. Eng. Chem.* **2002**, *56*, 40–52. [[CrossRef](#)]
40. Rankl, M.; Laib, S.; Seeger, S. Surface tension properties of surface-coatings for application in biodiagnostics determined by contact angle measurements. *Colloids Surfaces B Biointerfaces* **2003**, *30*, 177–186. [[CrossRef](#)]
41. Hong, S.; Kang, B.; Ahn, S.; Lee, M.J.; Lee, S.J.; Ma, Y.W.; Park, C.; Kang, M.S.; Shin, B.S. A study on micro/nano pattern replication using a hydroxyethyl cellulose polymer. *J. Korean Phys. Soc.* **2015**, *67*, 1966–1969. [[CrossRef](#)]
42. Hamdi, M.; Saleh, M.N.; Poulis, J.A. Improving the adhesion strength of polymers: Effect of surface treatments. *J. Adhes. Sci. Technol.* **2020**, *34*, 1853–1870. [[CrossRef](#)]

Disclaimer/Publisher’s Note: The statements, opinions and data contained in all publications are solely those of the individual author(s) and contributor(s) and not of MDPI and/or the editor(s). MDPI and/or the editor(s) disclaim responsibility for any injury to people or property resulting from any ideas, methods, instructions or products referred to in the content.